RESEARCH ARTICLE
PLANETARY SCIENCES

Earth and Planetary Physics
4: 105–110, 2020
doi: 10.26464/epp2020016

A rocky hill on the continuous ejecta of Ziwei crater revealed by the Chang'e-3 mission

ChunYu Ding[1], YuZhen Cai[1], ZhiYong Xiao[1,2,3*], and Yan Su[4]

[1]School of Atmospheric Sciences, Sun Yat-sen University, Zhuhai Guangdong 519082, China;

[2]State Key Laboratory of Lunar and Planetary Sciences, Space Science Institute, Macau University of Science and Technology, Macau 999078, China;

[3]Chinese Academy of Sciences Center for Excellence in Comparative Planetology, Hefei 230026, China;

[4]Key Laboratory of Lunar and Deep Space Exploration, National Astronomical Observatories, Chinese Academy of Sciences, Beijing 100012, China

Key Points:

- High-resolution topography and the channel 2 LPR data of Chang'e-3 are used together to estimate the relative permittivity of a lunar surface uplift
- This topographic uplift is located on top of the continuous ejecta deposits of Ziwei and the derived relative permittivity is ~9
- The subsurface materials close to the rim of Ziwei are dominated by basaltic boulders rather than excavated paleo-regolith

Citation: Ding, C. Y., Cai, Y. Z., Xiao, Z. Y., and Su, Y. (2020). A rocky hill on the continuous ejecta of Ziwei crater revealed by the Chang'e-3 mission. *Earth Planet. Phys.*, *4*(2), 105–110. http://doi.org/10.26464/epp2020016

Abstract: The Chinese Chang'e-3 mission landed close to the eastern rim of the ~450 m diameter Ziwei crater. Regional stratigraphy of the landing site and impact excavation model suggest that the bulk continuous ejecta deposits of the Ziwei crater are composed by Erathothenian-aged mare basalts. Along the traverse of the Yutu rover, the western segment features a gentle topographic uplift (~0.5 m high over ~4 m), which is spatially connected with the structurally-uplifted crater rim. Assuming that this broad topographic uplift has physical properties discontinuous with materials below, we use data returned by the high-frequency lunar penetrating radar onboard the Yutu rover to estimate the possible range of relative permittivity for this topographic uplift. Only when the relative permittivity is ~9 is the observed radar reflection consistent with the observed topography, suggesting that the topographic uplift is composed of basaltic blocks that were excavated by the Ziwei crater. This result is consistent both with the impact excavation model that predicts deeper basaltic materials being deposited closer to the crater rim, and with observation of numerous half-buried boulders on the surface of this hill. We note that this study is the first to use topography and radargram data to estimate the relative permittivity of lunar surface uplifts, an approach that has had many successful applications on Mars. Similar approaches can apply other ground penetrating radar data for the Moon, such as will be available from the ongoing Chang'e-4 mission.

Keywords: lunar penetrating radar; impact crater; ejecta deposits; Chang'e-3; permittivity; Moon

1. Introduction

The Chinese Chang'e-3 mission (i.e., CE-3) carried out the first in situ ground penetrating radar survey on the Moon (Su Y et al., 2014). The CE-3 landing site is ~50 m from the eastern rim of ~450 m diameter Ziwei crater, and the Yutu rover inspected a small area of the continuous ejecta deposits (Figure 1a; Xiao L et al., 2015).

Using data returned by high-frequency lunar penetrating radar (i.e., LPR), the relative permittivity of subsurface materials along the route of Yutu was estimated to be ~3 (Fa WZ et al., 2015; Lai JL et al., 2016), which is close to that of typical lunar regolith (Carrier III et al., 1991). This inversion result is consistent with the geological context of the landing area. Assuming that the final rim-to-rim diameter of simple craters is ~1.3 times that of the transient crater, and that the maximum excavation depth is ~1/10 of the transient crater diameter (Melosh, 1989), it can be inferred that the Ziwei crater has excavated materials from a depth of ~34.6 m. On the other hand, the pre-impact target of Ziwei is composed of a surface regolith layer and deeper competent basalts. This paleo-regolith layer was developed primarily from the Eratosthenian-aged mare basalts. Based on the morphology and reflectance spectra of small impact craters, previous studies have suggested that the median thickness of this paleo-regolith layer is ~8 m (Fa WZ et al., 2014) and that the Eratosthenian-aged mare basalts are 40–43 m thick (Qiao L et al., 2016). Therefore, the ejecta deposits from Ziwei probably originated mainly in the Eratosthenian-aged mare basalts.

On the other hand, impact excavation modeling predicts that deeper materials will be deposited closer to the crater rim (Melosh, 1989). Numerous meter-scale large blocks are visible on the wall and rim of Ziwei (Figure 1a; Xiao L, 2014), which is more-consistent with the larger excavation depth of Ziwei than the

Correspondence to: Z. Y. Xiao, xiaozhiyong@mail.sysu.edu.cn
Received 15 OCT 2019; Accepted 11 NOV 2019.
Accepted article online 04 DEC 2019.

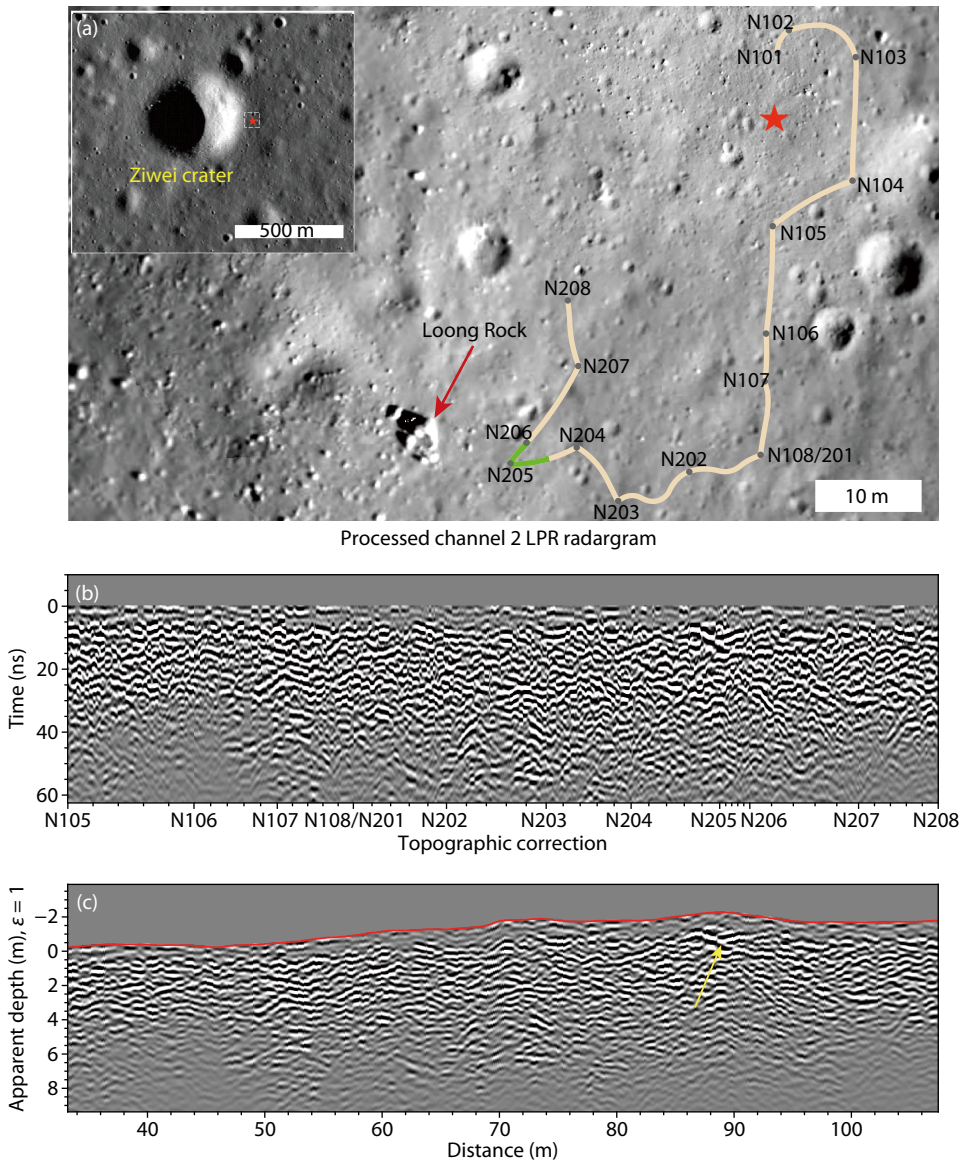

Figure 1. Radargram obtained by the high-frequency LPR onboard the Yutu rover. (a) Geological context of the Chang'e-3 landing site. The landing site (red star) is located in the eastern rim of Ziwei crater (~450 m in diameter). The solid line represents the route of the Yutu rover, which is ~107.4 m from the navigation point N101 to N208. The topographic uplift is denoted as the green segment along the route. The upper left inset is obtained by the Lunar Reconnaissance Orbit (Image ID: M102285549LE+RE), and the based image is acquired by the descent camera (Image ID: CE3_BMYK_LCAM-3006) on the Chang'e-3 lander. (b) Fully-processed radargram based on data obtained by the high-frequency LPR from the navigation point N105 to N208. The reflector from the lunar surface is identified at ~29 ns. (c) Radargram corrected based on the elevation along the route of Yutu. The yellow arrow points to the reflector that was interpreted as a crater floor by Feng JQ et al. (2017). The relative permittivity is assumed to be 1. The estimated apparent depth is shown in the *y*-axis; the *x*-axis denotes the travelling distances.

depth of the pre-impact regolith layer (i.e., ~34.6 m versus 8 m). Therefore, it is highly likely that at places closer to the rim of Ziwei, the surface materials should exhibit a larger relative permittivity due to the higher concentration of basaltic boulders.

Using high-resolution topography data obtained from the engineering team, Feng JQ et al. (2017) noticed that the western segment of Yutu's route had a slightly larger elevation. A radar reflection at shallow depth (Figures 1b and 1c) was interpreted to be caused by this topography high, but the physical properties of materials within the hill were not constrained (Feng JQ et al., 2017). Here we assume that the shallow radar reflection in the subsurface was indeed caused by the small topographic uplift. The possible range of relative permittivity of materials in this broad topographic uplift is constrained using two different methods. Our results prove that the surface materials close to the rim of Ziwei are dominated by basaltic boulders rather than excavated paleo-regolith.

2. Data and Method

2.1 Data

We use data returned by the high-frequency LPR onboard the

Yutu rover. The CE-3 LPR system consists of two channels. The Channel 1 LPR was worked at a center frequency of 60 MHz; its range resolution in regolith-like material is meter scale (Fang GY et al., 2014). The Channel 2 LPR has a designed frequency of 500 MHz and its range resolution is better than 0.3 m in lunar regolith (Fang GY et al., 2014). In total, the Channel 2 LPR obtained 2308 traces of valid data along the ~114 m long route (Xiao L et al., 2015). The LPR data are processed following the routine procedure used previously in many studies (e.g., Feng JQ et al., 2017), which is therefore not described here. Figure 1b shows the final radargram from the navigation points N105 to N208, where the zero position of the lunar surface is set to 29 ns (Feng JQ et al., 2017).

The CE-3 engineering team tracked the elevation of the Yutu rover along the route (see the red line shown in Figure 1c). The radargram is adjusted to reflect these topographic details; the result is shown in Figure 1c. The highest elevation along the route of Yutu is between the navigation points N204 to N206 (Figures 1c and 2a). Along the topographic profile, the region between navigation points N204 to N207 occurs as a broad topographic uplift, which is ~0.5 m high and ~4.2 m in width (Figure 1a and 2a). Below the highest elevation, the first radar reflection (yellow arrow in Figure 1c) was interpreted to be caused by the floor of a buried crater, considering the faint concave morphology (Figures 1c and 2), but possible reasons for this interpretation were not deciphered (Feng JQ et al., 2017). To deduce the possible range of relative permittivity for materials within the high-relief area, data from navigation points N204 to N207 are used in this study.

2.2 Methods

Two methods are used to deduce the relative permittivity of the topographic uplift; both methods have been applied on Mars using radar data, e.g., Watters et al. (2007) and Orosei et al. (2017) calculated the relative permittivity of Medusa Fossae Formation (MFF) and Lucus Planum on Martian surface using MARSIS (Mars Advanced Radar for Subsurface and Ionosphere Sounding) data, respectively. A similar method was applied to estimate the relative permittivity of MFF using SHARAD (SHAllow RADar) radar

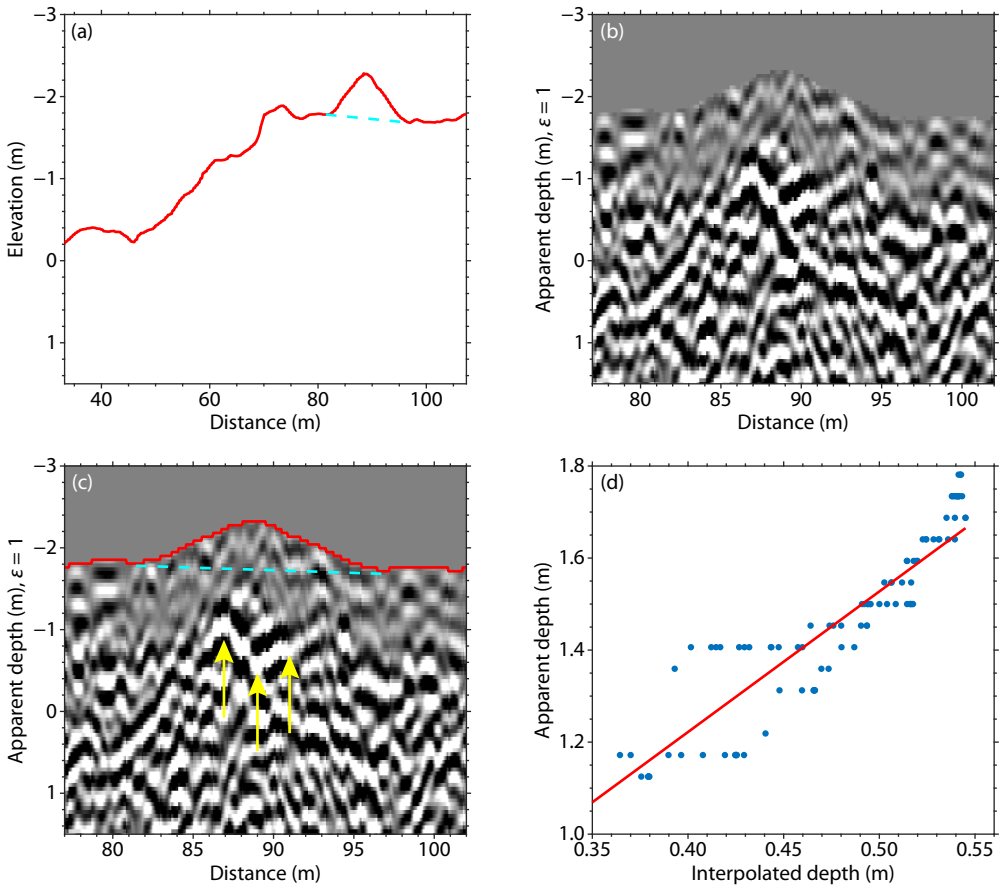

Figure 2. Estimation of the relative permittivity of materials in the high-relief area based on topography and radargram. (a) Topographic profile along the route of Yutu from navigation points N205 to N208, which corresponds to ~33.4 to 107.4 m from N101. The cyan dashed line connects the base points of the high-relief area. (b) Radargram for the area from navigation points N204 to N207. The apparent depth of $\varepsilon = 1$ is shown here. (c) Overlap of the radargram shown in panel (b) and the topographic profile shown in panel (a). The deduced relative permittivity should permit a good fit between the base of the topographic hill and the subsurface reflector. The cyan dashed line is the possible base position of the topographic uplift. (d) Deducing the relative permittivity of materials in the topographic hill based on the topography and the radargram. The apparent depths are extracted along the reflector, which are referred from the lunar surface (panel c). The interpolated depths are extracted from the topographic profile (panel a), which are referred to the highest elevation point. The slope of the best-fit between the apparent depths and the interpolated depths corresponds to the relative permittivity (red line; Equations (1) and (2)).

(Carter et al., 2009b). Both methods assume that the topographic uplift has different physical properties from those of deeper materials; thus, the base of this topographic hill (i.e., the cyan dashed line in Figure 2a) is assumed to have caused the first radar reflection (i.e., the yellow arrows in Figure 2c). The subsurface reflector is not symmetric in shape, as the left part is slightly shallower than the right part (Figure 2b). To avoid large uncertainty caused by manual extraction of the subsurface reflector (Figure 2b), we instead use a semi-automatic method to extract the reflector. This method checks each A-scan and automatically finds the peak position of the subsurface reflector.

2.2.1 Method 1

In radar sciences, the relative permittivity of materials (ε) is the ratio between apparent depths and actual depths in radargrams (Ulaby et al., 1986). The actual depth (d) of the subsurface reflector can be calculated using Equation (1):

$$d = \frac{c \cdot \tau}{2\sqrt{\varepsilon}}, \tag{1}$$

where c is the propagating speed of the electromagnetic waves in vacuum, and τ is the two-way traveling time. Using Equation (1), Equation (2) relates the apparent depth (d_a; assuming $\varepsilon = 1$) to the actual relative permittivity.

$$\varepsilon = \left(\frac{d_a}{d}\right)^2. \tag{2}$$

While the apparent depth can be extracted from the radargram (Figure 1b), the actual depth of the given radargram can be interpolated from the topographic data. Figure 2 shows the schematic illustration of constraining the relative permittivity using topography and apparent depth. Again, this estimate is based on the assumption that the base of the observed topographic uplift (the cyan dashed line in Figure 2a) is the cause (reflector) of the first radar reflection (Figure 2b).

2.2.2 Method 2

The second method used to deduce the possible range of relative permittivity is referred from Carter et al. (2009b); it is based on iterative comparison between the surface topography and calculated radargrams that assume different relative permittivity. Assuming that the observed reflector is equivalent to the base of the topographic hill, the likely relative permittivity should permit a good fit between the location of the reflector and the base of the topographic hill. Figure 3 shows the process of deriving the relative permittivity.

3. Results

Both of the above methods yield a relative permittivity of ~9 for this topographic uplift. Using the method introduced in Section 2.2.1, the apparent depths along the reflector are extracted and compared with the depths along the base of the hill (Figure 2d). The scatter diagram shows correlation between apparent depths and interpolated depths. Employing the data-fitting linear function shown in Equation (2), we find the best-fit slope to be ~3.05, which with 95% confidence implies that the inversed relative permittivity of the convex deposit is 9.29 ± 0.38. Using the method introduced in Section 2.2.2, we have tested arelative permittivity range from 1 to 9 for the radargram. The comparison between the radargrams and the surface topography shows that if ε = 1–5 the subsurface reflector in the radargram is deeper than the base of the topographic hill (Figures 3b–3d). If ε = 7, the left of the reflector matches well with the base of the topographic hill (Figure 3e),

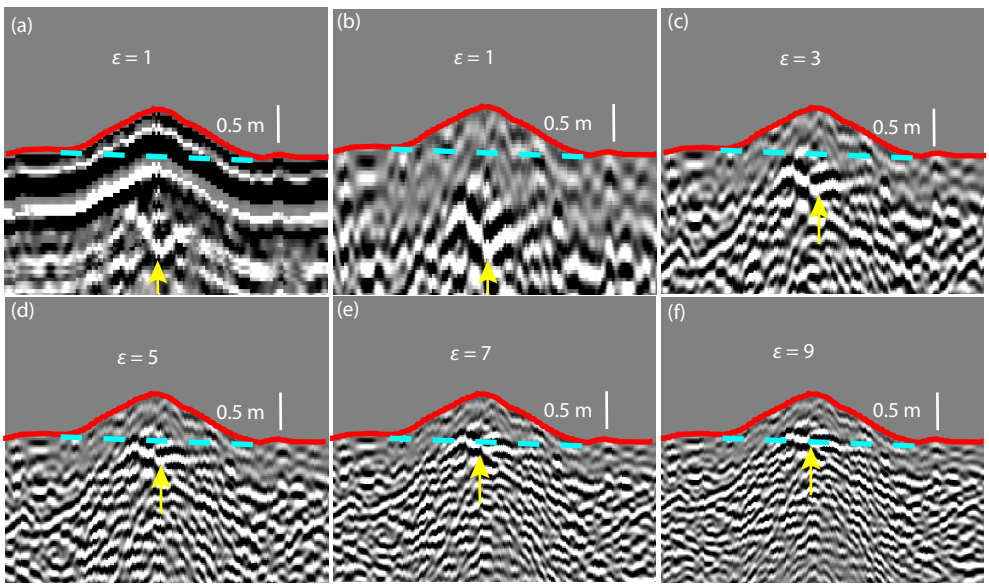

Figure 3. Process of deriving the relative permittivity for the topographic hill. Data in the radargrams are identical with those used in the Figure 2b. The red lines are the surface topography, the cyan dashed lines denote the possible base of this topographic hill. (a) Radargram plotted from the raw data (assuming relative permittivity ε = 1) after correcting the topography. The yellow arrow points to the reflector, which is assumed to be caused by the discontinuity at the base of the topographic uplift. Note that the reflector is located beyond the saturation zone of reflected signals. Panels (b)–(f) are fully-processed radargrams that are plotted using different values of relative permittivity. The comparison between the radargrams and the topography suggests that only when ε = 7–9 does the reflector appear to be at the base of the topographic hill.

but the right half of the reflector is slightly lower. The best match occurs when ε is assumed to be equal to 9 (Figure 3f). Therefore, both methods suggest that the relative permittivity for materials within the topographic hill is most likely ~9.

4. Discussion and Conclusion

A relative permittivity of ~9 for the topographic uplift supports both the geologic context and crater excavation model (Section 1) that the ~0.5 m thick materials are dominated by basaltic boulders. Basaltic rocks returned by Apollo samples have relative permittivity of 5.1–11.6 (Olhoeft and Strangway, 1975), and typical lunar regolith has a relative permittivity of ~3 (Carrier III et al., 1991). On the other hand, this topographic uplift is part of the continuous ejecta deposits of Ziwei, and to the west it is connected with the blocky crater rim (Figure 4a and 4b). Numerous meter-scale boulders are visible along the route from N204 to N207 (Figures 4c and 4d). Therefore, a blocky topographic uplift is consistent with the surface morphology.

The methods used in this study have recently been successfully applied in studies of Mars geology (Watters et al., 2007; Carter et al., 2009a, b; Orosei et al., 2017). The combined use of high-resolution topographic and radargram data in deducing the possible range of relative permittivity is indicated for future lunar geology research, such as in the ongoing Chang'e-4 mission.

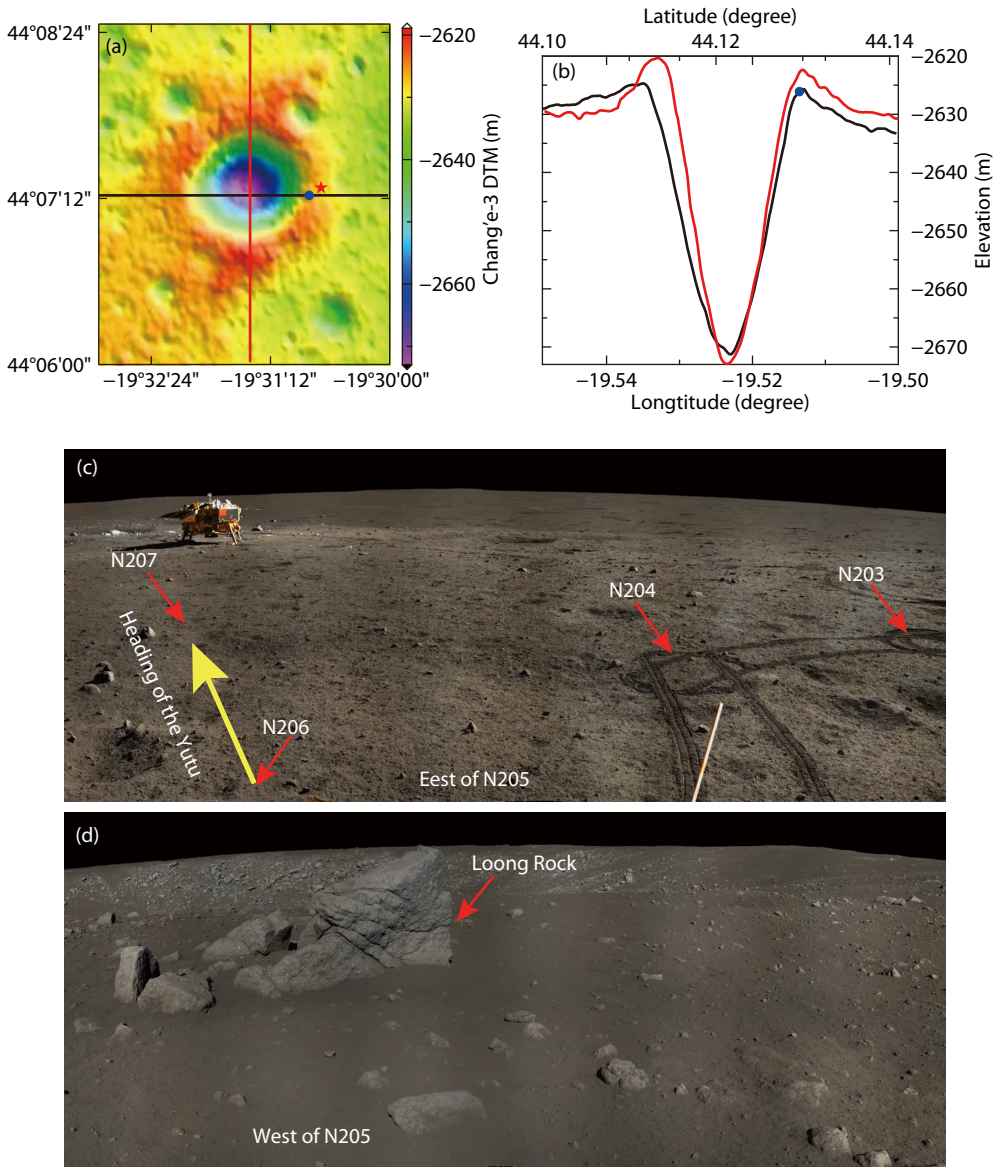

Figure 4. The topographic hill is most likely formed by rock piles that were excavated by the Ziwei crater. (a) Digital elevation model of the Chang'e-3 landing site, constructed by the Lunar Reconnaissance Orbiter Camera team (http://wms.lroc.asu.edu/lroc/view_rdr/NAC_DTM_CHANGE3). The black and red solid lines correspond to two topographic profiles (plane b) across the Ziwei crater. The red star denotes the CE-3 landing site, and the blue dot mark position of the topographic uplift. The topographic uplift is part of the continuous ejecta deposits of Ziwei. (b) Topographic profiles across the Ziwei crater. (c) and (d) are images obtained by the panoramic camera onboard the Yutu rover, which show the blocky surface from the navigation point N204 to N207. Denotations in the photos are the navigation points.

Availability of Data and Materials

Source codes and data used in this study can be open access on the website: https://github.com/dingchunyu1989/Ding-et-al.-2019-A-rock-hill-at-CE-3-landing-site.

Acknowledgments

The LPR data used in this study are available at the Ground Application System of Lunar Exploration, NAOC (http://moon.bao.ac.cn). This work is supported by the National Natural Science Foundation of China (41773063, 41525015 and 41830214), the Science and Technology Development Fund of Macau (0042/2018/A2), and the Opening Fund of the Key Laboratory of Lunar and Deep Space Exploration, CAS (no.ldse201702).

References

Carrier Ⅲ, W. D., Olhoeft, G. R., and Mendell, W. (1991). Physical Properties of the lunar Surface. Lunar Sourcebook: A User's Guide to the Moon, 475-594.Cambridge, England: Cambridge University Press.

Carter, L. M., Campbell, B. A., Holt, J. W., Phillips, R. J., Putzig, N. E., Mattei, S., Seu, R., Okubo, C. H., and Egan, A. F. (2009a). Dielectric properties of lava flows west of Ascraeus Mons, Mars. *Geophys. Res. Lett.*, *36*(23), L23204. https://doi.org/10.1029/2009gl041234

Carter, L. M., Campbell, B. A., Watters, T. R., Phillips, R. J., Putzig, N. E., Safaeinili, A., Plaut, J. J., Okubo, C. H., Egan, A. F., … Orosei, R. (2009b). Shallow radar (SHARAD) sounding observations of the Medusae Fossae Formation, Mars. *Icarus*, *199*(2), 295–302. https://doi.org/10.1016/j.icarus.2008.10.007

Fa, W. Z., Zhu, M. H., Liu, T. T., and Plescia, J. B. (2015). Regolith stratigraphy at the Chang'E-3 landing site as seen by lunar penetrating radar. *Geophys. Res. Lett.*, *42*(23), 10179–10187. https://doi.org/10.1002/2015gl066537

Fa, W. Z, Liu, T. T, Zhu, M. H., and Haruyama, J. (2014). Regolith thickness over Sinus Iridum: Results from morphology and size-frequency distribution of small impact craters. *J. Geophys. Res.*, *119*(8), 1914–1935. https://doi.org/10.1002/2013JE004604

Fang, G. Y., Zhou, B., Ji, Y. C., Zhang, Q. Y., Shen, S. X., Li, Y. X., Guan, H. F., Tang, C. J., Gao, Y. Z., … Wang, S. Z. (2014). Lunar penetrating radar onboard the Chang'e-3 mission. *Res. Astron. Astrophys.*, *14*(12), 1607–1622. https://doi.org/10.1088/1674-4527/14/12/009

Feng, J. Q., Su, Y., Ding, C. Y., Xing, S. G., Dai, S., and Zou, Y. L. (2017). Dielectric properties estimation of the lunar regolith at CE-3 landing site using lunar penetrating radar data. *Icarus*, *284*, 424–430. https://doi.org/10.1016/j.icarus.2016.12.005

Lai, J. L., Xu, Y., Zhang, X. P., and Tang, Z. S. (2016). Structural analysis of lunar subsurface with Chang'E-3 lunar penetrating radar. *Planet. Space Sci.*, *120*, 96–102. https://doi.org/10.1016/j.pss.2015.10.014

Melosh, H. J. (1989). Impact Cratering: A Geologic Process. New York: Oxford Univ. Press.

Olhoeft, G. R., Strangway, D. W. (1975). Dielectric properties of the first 100 meters of the Moon. *Earth Planet. Sci. Lett.*, *24*(3), 394–404. https://doi.org/10.1016/0012-821X(75)90146-6

Orosei, P., Rossi, A. P., Cantini, F., Caprarelli, G., Carter, L. M., Papiano, I., Cartacci, M., Cicchetti, A., and Noschese, R. (2017). Radar sounding of Lucus Planum, Mars, by MARSIS. *J. Geophys. Res.*, *122*(7), 1405–1418. https://doi.org/10.1002/2016je005232

Qiao, L., Xiao, Z. Y., Zhao, J. N., and Xiao, L. (2016). Subsurface structures at the Chang'e-3 landing site: interpretations from orbital and in-situ imagery data. *J. Earth Sci.*, *27*(4), 707–715. https://doi.org/10.1007/s12583-015-0655-3

Su, Y., Fang, G. Y., Feng, J. Q., Xing, S. G., Ji, Y. C., Zhou, B., Gao, Y. Z., Li, H., Dai, S., … Li, C. L. (2014). Data processing and initial results of Chang'e-3 lunar penetrating radar. *Res. Astron. Astrophys.*, *14*(12), 1623–1632. https://doi.org/10.1088/1674-4527/14/12/010

Ulaby, F. T., Moore, M. K., and Fung, A. K. (1986). Microwave Remote Sensing: Active and Passive, Vol 3. Norwood, Mass: Artech House.

Watters, T. R., Campbell, B., Carter, L., Leuschen, C. J., Plaut, J. J, Picardi, G., Orosei, R., Safaeinili, A., Clifford, S. M., … Stofan, E. R. (2007). Radar sounding of the Medusae fossae formation mars: equatorial ice or dry, low-density deposits?. *Science*, *318*(5853), 1125–1128. https://doi.org/10.1126/science.1148112

Xiao, L. (2014). China's touch on the Moon. *Nat. Geosci.*, *7*(6), 391–392. https://doi.org/10.1038/ngeo2175

Xiao, L., Zhu, P. M., Fang, G. Y, Xiao, Z. Y., Zou, Y. L., Zhao, J. N., Zhao, N., Yuan, Y. F, Qiao, L., … Gao, Y. Z. (2015). A young multilayered terrane of the northern Mare Imbrium revealed by Chang'E-3 mission. *Science*, *347*(6227), 1226–1229. https://doi.org/10.1126/science.1259866